Pramana – J. Phys. (2016) 87: 98
DOI 10.1007/s12043-016-1304-9

Real-time stress detection of monocrystalline silicon by laser irradiation using Mach–Zehnder interferometry

MING GUO[1,2], GUANGYONG JIN[1,*], YONG TAN[1], WEI ZHANG[1], MINGXIN LI[1], JIXING CAI[1] and YAO MA[1]

[1]School of Science, Changchun University of Science and Technology, Changchun 130022, China
[2]College of Optical and Electronical Information, Changchun University of Science and Technology, Changchun 130022, China
*Corresponding author. E-mail: lasercust@sina.com

MS received 6 July 2015; revised 11 March 2016; accepted 18 April 2016; published online 12 November 2016

Abstract. The effect of changes in laser-induced stress upon irradiation of monocrystalline silicon was studied in detail using Mach–Zehnder interferometer, high speed camera and computer processing system, real-time detection of stress distribution and stress evolvement under different laser fluences and pulse widths. After irradiation, the changes of interference fringes were used to calculate the stress value. The results show that the stresses increased with the increase of the laser fluence. The formation of stress could be explained using thermoelastic theory. The cleavage plane's dislocation appears in the following sequence: (1 1 1) plane appears and then the dislocation slip of (1 1 0) cleavage plane appears. In addition, it is found that cleavage plane of (1 1 1) mainly exist in the spot and cleavage plane of (1 1 0) mainly exists in the vicinity of spot radius. Stress areas mainly exist in the thin layer on the surface of silicon. Furthermore, stress field was analysed by the finite-element method to get a better understanding of the formation and distribution of stress. Under the same experimental conditions, the numerical results are in agreement with the experimental values.

Keywords. Monocrystalline silicon; Mach–Zehnder interferometer; stress.

PACS Nos 42.55.−f; 42.70.−a

1. Introduction

Silicon is brittle at room temperature [1]. It attracts a great deal of attention because of its special properties such as large specific surface area, high reactivity, diverse topological structure and photoelectroluminescence [2]. On the one hand, in laser processing, in order to produce perfect surface quality, we need to fully understand the mechanism of ductility in a brittle material [3], which allows us to suppress brittle fracture and decrease surface damage. On the other hand, in complex devices and the thin film materials, problems often arise from mechanical strain and stress [4]. The reliability issue of mechanical stress becomes even more crucial with the development of super-large-scale integration technology towards the deep-submicron regime, and the measurement of stress in silicon turns out to be a significant subject because monocrystalline silicon is a common material.

Stress problems are pervasive and critical in silicon technology. Nowadays, strain engineering is quite extensively used in the microelectronics industry [5]. Although the technology of silicon fracture has been studied extensively in recent years [6], there used to be few demonstrable real-time detections on stress distribution. Thermal stress is one of the major factors for generating dislocations [7]. Dislocations are easily generated in silicon when the effective stress exceeds the critical resolved shear stress of the material.

In laser-irradiated monocrystalline silicon, the temperature increases due to the absorption of laser energy, temperature gradient and thermal stress and strain may be formed in that region and its vicinity. There are several measurement schemes now for detecting residual stress [8], among which X-ray diffraction, neutron diffraction, magnetic method, ultrasonic method and the indentation strain method are common. Though being the perfect theory, ray theory can only be used to measure

surface stress because the ray may damage materials, which greatly limits its usage. Magnetic method measures according to the change between the stress and the magnetization curve. Therefore, this application is also very limited. Impact indentation strain method requires laser to be close to the back of the material. However, it may result in measurement errors if the surface strain is too small when laser interacts with the material. All these methods cannot quickly respond to the change of stress caused by short pulse laser. Hence, these methods cannot do an accurate measurement of stress and strain evolution during laser interactions with materials. Mach–Zehnder interferometry has realized the real-time stress detection of monocrystalline silicon by laser irradiation. This work demonstrates the potential of stress measurement technology being used to improve accuracy and efficiency, and demonstrates the advantages of low-cost non-destructive testing.

With the development of modern computer technology, numerical simulation has been developed as a powerful tool for analysing the generation and distribution of stress. In this paper, an analytical model was proposed to simulate stress generation during irradiation by the laser.

2. Numerical simulation

2.1 *Numerical model*

We numerically calculated the stress process of the millisecond laser-irradiated silicon by finite element method. A three-dimensional analysis is presented in the figure below. In the model, the laser beam which strikes on the surface of silicon is in the shape of Gaussian distribution, as shown in figure 1. Physical parameters of monocrystalline silicon and laser are expressed in table 1.

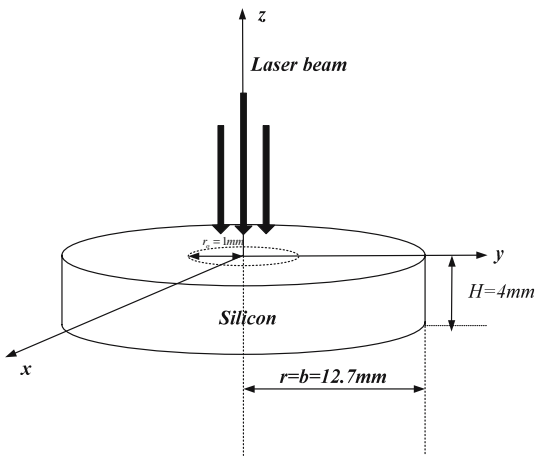

Figure 1. Schematic diagram of the process.

The thermal conductive equation [13]:

$$\rho c\frac{\partial T(x,y,z,t)}{\partial t} = \frac{\partial}{\partial x}\left(k\frac{\partial T(x,y,z,t)}{\partial x}\right) + \frac{\partial}{\partial y}\left(k\frac{\partial T(x,y,z,t)}{\partial y}\right) + \frac{\partial}{\partial z}\left(k\frac{\partial T(x,y,z,t)}{\partial z}\right) + I,$$

where L is the latent heat of the melt, c is the heat capacity, I is the heat resource phase from the laser heat deposition and

$$I = \alpha(T)(1 - R(T))I_0 f(r)g(t)\mathrm{e}^{-\alpha(T)z},$$

where $g(t)$ and $f(r)$ are the temporal and spatial distributions of the pulse laser. Here, we choose Gaussian distribution for $f(r)$

$$f(r) = \mathrm{e}^{-2r^2/r_0^2}, \quad r = \sqrt{x^2 + y^2}.$$

The initial condition is

$$T_0 = 300\ \mathrm{K}$$
$$-k\frac{\partial T(x,y,z,t)}{\partial x}\bigg|_{x=b} = 0,$$
$$-k\frac{\partial T(x,y,z,t)}{\partial y}\bigg|_{y=b} = 0,$$
$$-k\frac{\partial T(x,y,z,t)}{\partial z}\bigg|_{z=h,z=0} = 0.$$

It is feasible to simulate the stress process of silicon based on thermoelastic theory. The thermoelastic equation [14] can be described as

x direction:

$$\nabla^2 u_x + \frac{1}{1-2\mu}\frac{\partial \varepsilon}{\partial x} - \frac{2(1+\mu)}{1-2\mu}\beta\frac{\partial T}{\partial x} = 0. \tag{1}$$

y direction:

$$\nabla^2 u_y + \frac{1}{1-2\mu}\frac{\partial \varepsilon}{\partial y} - \frac{2(1+\mu)}{1-2\mu}\beta\frac{\partial T}{\partial y} = 0. \tag{2}$$

z direction:

$$\nabla^2 u_z + \frac{1}{1-2\mu}\frac{\partial \varepsilon}{\partial z} - \frac{2(1+\mu)}{1-2\mu}\beta\frac{\partial T}{\partial z} = 0, \tag{3}$$

where u_x, u_y and u_z are the displacement components of x, y, z, Poisson ratio $\mu = 0.28$, linear thermal expansion coefficient $\beta = 2.0 \times 10^{-5}\ \mathrm{K}^{-1}$.

The initial conditions are:

$$u_x|_{t=0} = 0, \quad u_y\big|_{t=0} = 0, \quad u_z|_{t=0} = 0 \tag{4}$$

$$\frac{\partial u_x}{\partial t}\bigg|_{t=0} = 0, \quad \frac{\partial u_y}{\partial t}\bigg|_{t=0} = 0, \quad \frac{\partial u_z}{\partial t}\bigg|_{t=0} = 0. \tag{5}$$

Table 1. Physical parameters of monocrystalline silicon and laser [9–12].

Parameters	Symbol	Dimension	Value or expression
Size			
Radius	r	m	1.27×10^{-2}
Thickness	H	m	4×10^{-3}
Absorption coefficient	α_s	m^{-1}	$1023 \times (T/273)^4$
	α_l	m^{-1}	8.6×10^7
Thermal conductivity	k_s	$W{\cdot}m^{-1}K^{-1}$	$22.23 + 422.52 \times \exp(-T/255.45)$
	k_l	$W{\cdot}m^{-1}K^{-1}$	62
Heat capacity	C_s	$J{\cdot}kg^{-1}{\cdot}K^{-1}$	$352.43 + 1.78 \times T - 2.21 \times 10^{-3}T^2 - 1.3 \times 10^{-6}T^3 - 2.83 \times 10^{-10}T^4$
	C_l	$J{\cdot}kg^{-1}{\cdot}K^{-1}$	1021.84
Density	ρ_s	$kg{\cdot}m^{-3}$	$2330 - 2.19 \times 10^{-2}T$
	ρ_l	$kg{\cdot}m^{-3}$	$2540 - 2.19 \times 10^{-2}T - 1.21 \times 10^{-5}T^2$
Young's modulus	E	GPa	160
	C	GPa	$\mathbf{C} = \begin{pmatrix} C_{11} & C_{12} & C_{12} & & & \\ C_{12} & C_{11} & C_{12} & & & \\ C_{12} & C_{12} & C_{11} & & & \\ & & & C_{44} & & \\ & & & & C_{44} & \\ & & & & & C_{44} \end{pmatrix}$ $C_{11} = 165.7, C_{12} = 63.9, C_{44} = 76.9$
Reflectivity	R	1	$R_s = 0.33/R_l = 0.72$
Melting point	T_m	K	1687
Boiling point	T_v	K	3175
Spot radius	r_0	mm	1
Repetition rate	f	Hz	10

s indicates solid state, l indicates liquid state.

Boundary conditions: As the edge of monocrystalline silicon is stationary, top and bottom surfaces of monocrystalline silicon have free boundary conditions, change them into fixed boundary conditions:

$$u_x|_{r=b} = 0, \quad u_y|_{r=b} = 0, \quad u_z|_{r=b} = 0. \tag{6}$$

Strain vector can be obtained according to the geometric equations:

$$\begin{pmatrix} \varepsilon_x \\ \varepsilon_y \\ \varepsilon_z \\ \gamma_{xy} \\ \gamma_{yz} \\ \gamma_{zx} \end{pmatrix} = \begin{pmatrix} \dfrac{\partial u_x}{\partial x} \\ \dfrac{\partial u_y}{\partial y} \\ \dfrac{\partial u_z}{\partial z} \\ \dfrac{\partial u_y}{\partial x} + \dfrac{\partial u_x}{\partial y} \\ \dfrac{\partial u_z}{\partial y} + \dfrac{\partial u_y}{\partial z} \\ \dfrac{\partial u_x}{\partial z} + \dfrac{\partial u_z}{\partial x} \end{pmatrix}. \tag{7}$$

Stress vector can be obtained according to the Hooke law:

$$\boldsymbol{\sigma} = \mathbf{C}(\boldsymbol{\varepsilon} - \boldsymbol{\varepsilon}_0) \tag{8}$$

$$\boldsymbol{\sigma} = (\sigma_x \quad \sigma_y \quad \sigma_z \quad \tau_{xy} \quad \tau_{yz} \quad \tau_{zx})^T \tag{9}$$

$$\boldsymbol{\varepsilon} = (\varepsilon_x - a_0T \quad \varepsilon_y - a_0T \quad \varepsilon_z - a_0T \quad \varepsilon_{xy} \quad \varepsilon_{yz} \quad \varepsilon_{zx})^T \tag{10}$$

$$\mathbf{C} = \begin{pmatrix} C_{11} & C_{12} & C_{12} & & & \\ C_{12} & C_{11} & C_{12} & & & \\ C_{12} & C_{12} & C_{11} & & & \\ & & & C_{44} & & \\ & & & & C_{44} & \\ & & & & & C_{44} \end{pmatrix}. \tag{11}$$

When selecting x, y, z directions of axes consistent with [1 0 0], [0 1 0], [0 0 1] directions of silicon, the experiment showed the following values: $C_{11} = 165.7$ GPa, $C_{12} = 63.9$ GPa, $C_{44} = 76.9$ GPa.

2.2 *Numerical results and analysis*

Due to the anisotropic characteristics of monocrystalline silicon's elastic modulus, there are many stress components according to different cleavage planes. In these stress components, the shear stress of [1 1 0] and [1 1 1] directions play a major role in the thermal stress damage because the two stress components are the root causes of dislocation in the lattice structure, producing lattice defects in monocrystalline silicon. We get figures 2–8 when the number of pulses (NP) = 1, $E_p = 10.1\ \mathrm{J/cm^2}$, $\tau_p = 1.0$ ms, $f = 10$ Hz.

The maximum shear stress of the [1 1 0] direction appears near the spot radius. But it does not have the characteristics of axial symmetry distribution. For monocrystalline silicon, the maximum shear stress intensity of the [1 1 0] distribution appears on the [1 1 0] and [$\bar{1}$ 1 0] directions. According to the distribution characteristics of shear stress in the [1 1 0] direction, if shear stress damage of [1 1 0] direction appears, then the stress damage morphology should be cross-shaped.

The spatial distribution of the [1 1 1] direction shear stress has the characteristics of axial symmetry and the stress in the centre of spot is the largest. According to the distribution characteristics of shear stress in the [1 1 1] direction, the shorter the distance to the centre of the spot is, the more obvious the crack is.

When the temperature is high enough, silicon cleavage takes place along the cleavage plane, produces cleavage dislocation and provides initiation points for brittle fracture according to the results of numerical simulation on the thermal stress damage (crack) of silicon. As the dislocation region caused by shear stress and the laser thermal damage region coincides, the dislocations of the overlapped regions can be eliminated by the fusion of thermal damage, vapourization, sputtering, and ablation. In regions other than thermally damaged regions, there are two cleavage dislocations along the (1 1 0) and (1 1 1) planes.

As the time of laser irradiation increases, shear stress intensity of the [1 1 0] direction increases rapidly. The maximum radial stress occurs in the vicinity of the spot. When the shear stress of the [1 1 0] direction is larger than the shear yield strength, silicon atoms will slip along the (1 1 0) cleavage plane, then dislocations are produced and dislocation lines appear on the silicon surface (1 0 0) plane. As the time of laser irradiation increases, the depth of dislocation extends inward. According to the distribution characteristics of the [1 1 1] direction shear stress along the radial direction, the initial dislocation tends to appear on the edge of the spot.

The axial distribution of [1 1 0] direction stress at different times are shown in figure 4b. The axial stress distribution is steeper and stress gradient is much larger when Z distance becomes longer. The maximum axial stress only appears in the centre of the spot, but the stress strength is about two orders of magnitude smaller

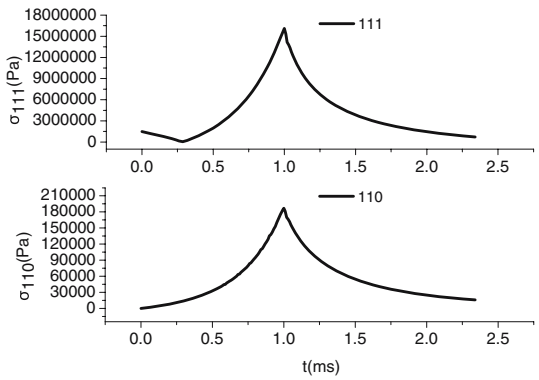

Figure 3. The stress evolution of the irradiated centre in the [1 1 0] and [1 1 1] directions.

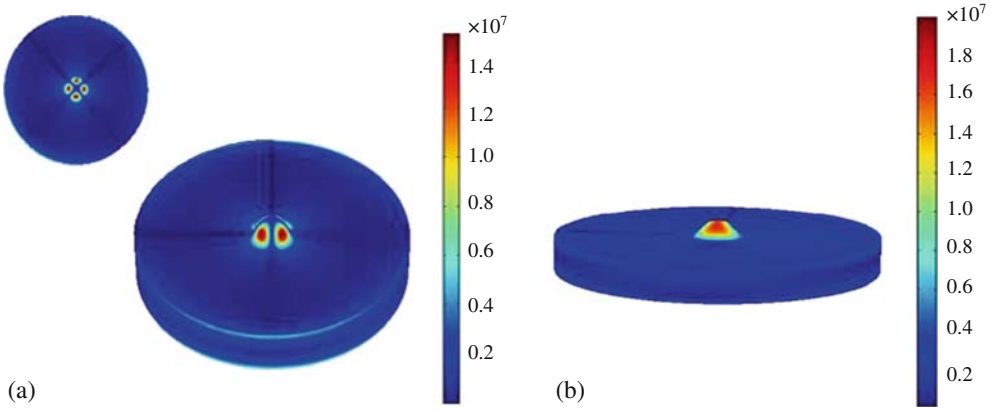

Figure 2. Three-dimensional stress distribution maps of silicon after laser irradiation. (**a**) Shear stress of [1 1 0] direction and (**b**) shear stress of [1 1 1] direction.

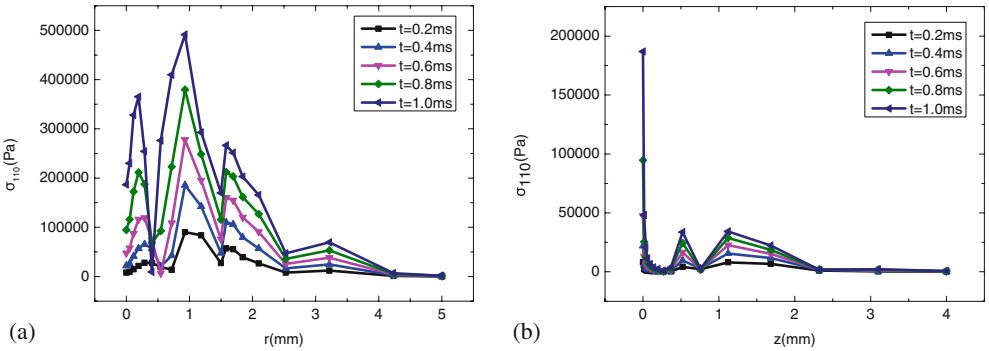

Figure 4. The [1 1 0] direction stress distributions at different times. (**a**) Radial and (**b**) axial distributions.

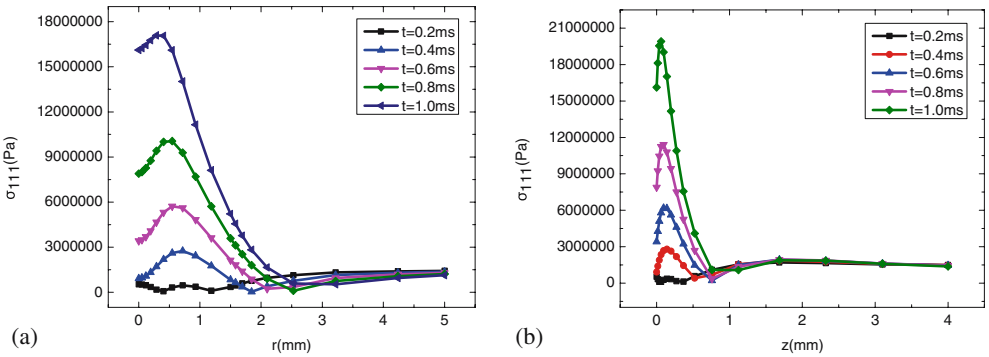

Figure 5. (**a**) Radial and (**b**) axial stress of [1 1 1] direction distributions at different times.

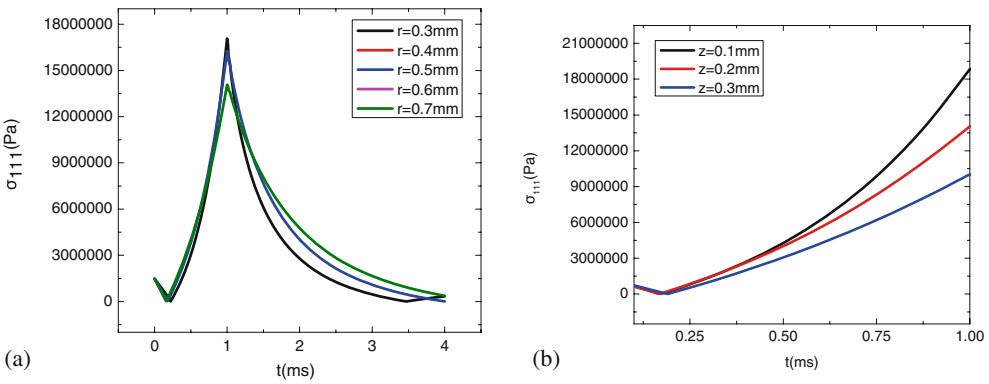

Figure 6. Profiles of [1 1 1] direction stress vs. time of irradiation in different positions of (**a**) radial and (**b**) axial stress.

than the shear yield strength, hence, it cannot produce dislocation on silicon.

The radial and axial stress of the [1 1 1] direction distributions at different time are shown in figure 5. Shear stress of the [1 1 1] direction is in the shape of approximate Gaussian distribution on radial direction and maximum stress appears in the centre of laser action. As shown in figure 4, shear stress intensity of the [1 1 1] direction is almost one order of magnitude bigger than the [1 1 0] direction. So, the order of dislocation of the cleavage plane is: (1 1 1) cleavage plane comes first, and then the dislocation slip of the (1 1 0) cleavage plane appears. In addition to the different dislocation times, the locations of the two dislocations are also different: cleavage plane of (1 1 1) mainly exists in the spot and cleavage plane of (1 1 0) mainly exists in the vicinity of spot radius.

Profiles of the [1 1 1] direction stress vs. irradiated time in different radial and axial positions are shown in figure 8. During the instant of laser effect, a small stress of about 1×10^6 Pa is produced in the spot radius because of the increase in temperature caused by the absorption of laser energy. Due to the relaxation effect, it is quickly reduced to 0 Pa at about 1.79×10^{-4} s. As the laser irradiation time increases, the absorption of laser energy increased and the different positions of stress value increases. When the distance from the centre is longer, the slope of the curve becomes smaller

and the increase in amplitude becomes slower. All locations reach maximum stress at the end of the laser effect. As the spatial distribution of the energy is Gaussian, the maximum stress decreases when the distance from the irradiated centre increases.

With the increase of the laser energy density, the maximum stress of the irradiated centre increases. The distribution of stress [1 1 1] along the radial direction is approximately of the Gaussian shape. When laser fluence is 47.8 J/cm^2, surface stress of the laser-irradiated centre is about 4.5×10^8 Pa. However, when it becomes only 2.5×10^{-4} m away from the silicon surface, the stress of the axial position drops to 3.1×10^7 Pa and reduces one order of magnitude. It can be seen that stress areas mainly exist in the thin layer on the surface of silicon.

From figures 9–11, we can see that the amount of time for the stress to reach the maximum increases and the maximum stress decreases with the increase of pulse width because of the decrease of laser power density.

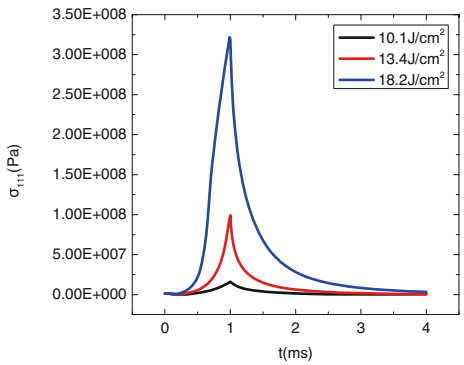

Figure 7. Profiles of [1 1 1] direction stress of irradiated centre vs. irradiated time under different laser fluences.

3. Experimental details

3.1 *Experimental set-up*

The experimental device which is used to measure the stress of monocrystalline silicon is shown in figure 12. The 1064 nm laser source is Meyer-100 of Beam-tech Optronics Co. The repetition frequency is 10 Hz. Laser pulse width can vary from 0.5 ms to 3 ms. In experiments, the laser pulse width is selected as 1 ms, 1.5 ms, 2 ms and 2.5 ms respectively. A laser beam with a near Gauss power distribution was focussed on silicon. The radius of the irradiation spot is 1 mm. We

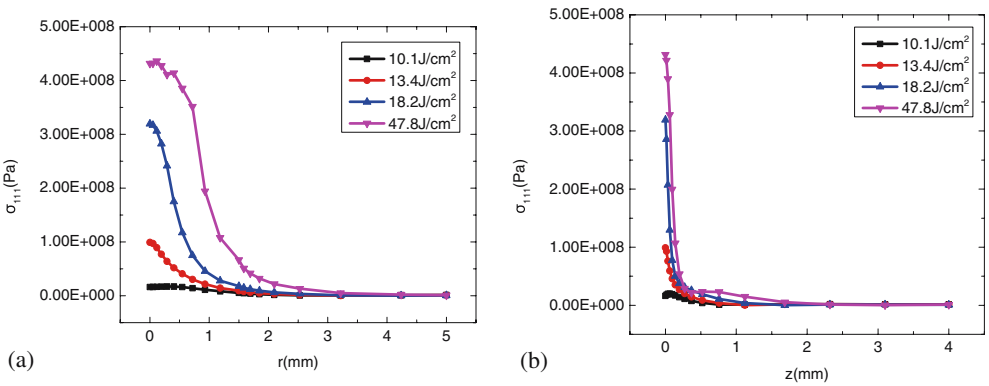

Figure 8. Profiles of [1 1 1] direction stress vs. (**a**) radial and (**b**) axial positions under different laser fluences.

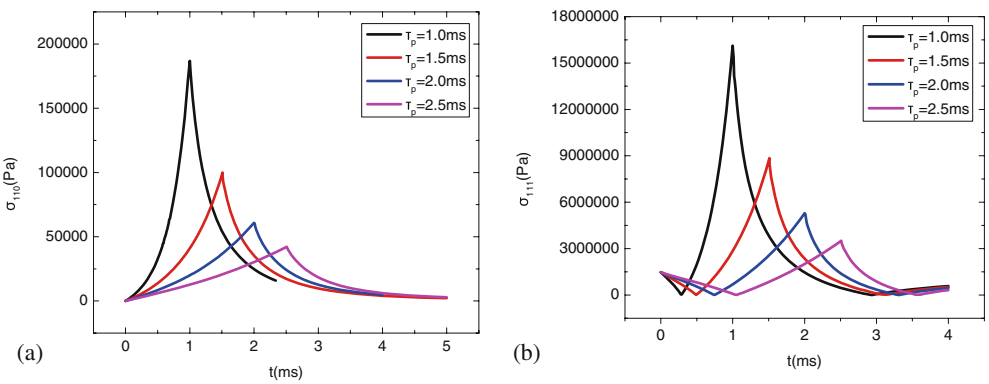

Figure 9. Profiles of stress vs. time of irradiation under different pulse widths. (**a**) [1 1 0] and (**b**) [1 1 1] directions.

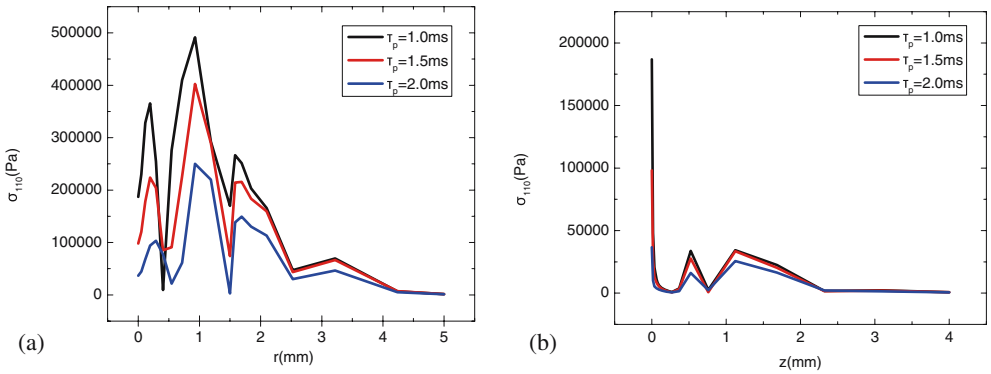

Figure 10. Profiles of [1 1 0] direction stress vs. (**a**) radial and (**b**) axial positions under different pulse widths.

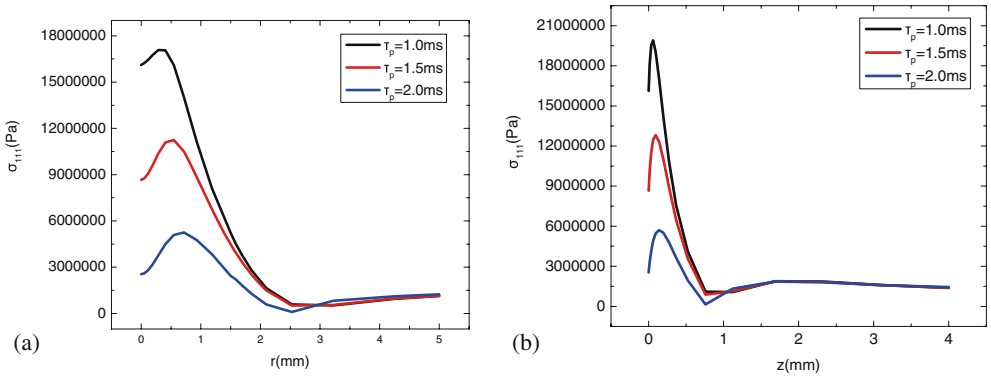

Figure 11. Profiles of [1 1 1] direction stress vs. (**a**) radial and (**b**) axial positions under different pulse widths.

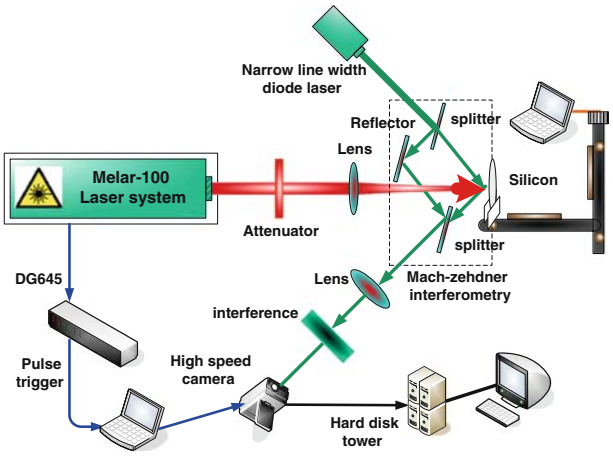

Figure 12. Schematic diagram of the method for producing and observing stress on monocrystalline silicon.

adjust the incident laser fluence by inserting the attenuator and lens in the beam path. The probe beam is divided into two parts by the beam splitter. One beam irradiates the monocrystalline silicon and the spot size is bigger than the spot irradiated. The other beam irradiates the mirror. Then the two beams combine into one after reflection. The interference fringes will be formed after the lens focus. The wavelength of the narrow linewidth diode laser is 532 nm, linewidth is less than 0.7 nm, the frame rate of high speed camera is more than 10000 which is triggered synchronously with laser.

The silicon wafers (4 mm thick, 25.4 mm diameter, single-side-polished (1 0 0)) are set on three-axis translation stages, which are put in acetone and methanol to be cleaned for 15 min by ultrasonic, the surface drops are purged by N_2, and then put into the low-temperature drying box to be dried slowly in low temperature. The experiment is performed at room temperature in air under normal atmospheric pressure, with the relative humidity being 50%.

3.2 *Experimental results and analysis*

Interference pattern of the structure found on silicon irradiated at different times as shown in figure 13. The stress can be calculated according to figure 13. The maximum radial stress measured by experiment is 2.86×10^5 Pa; axial stress is 1.1×10^5 Pa. The maximum radial stress of the simulation calculated is 4.4×10^5 Pa; axial stress is 3.89×10^5 Pa (figure 14).

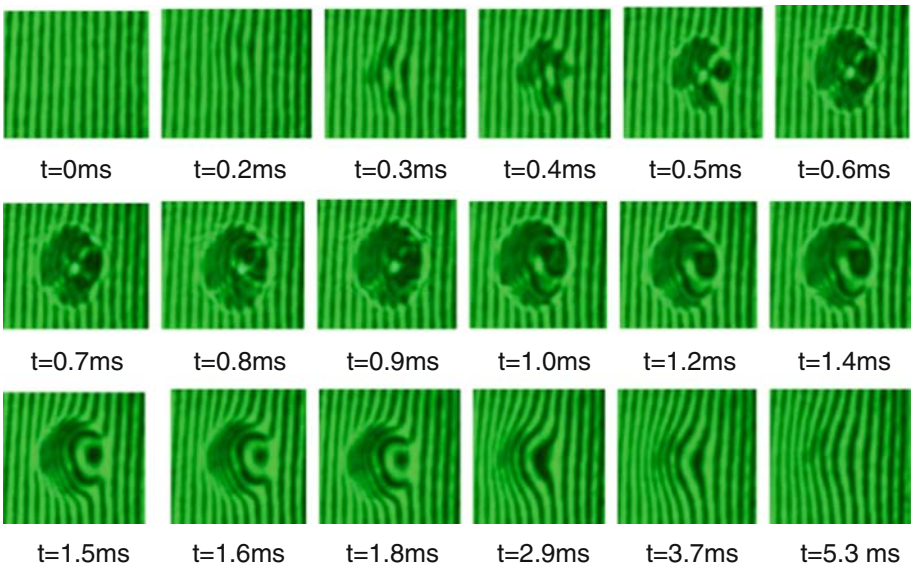

Figure 13. Interference pattern of the structure found on silicon irradiated at different times ($E_p = 10.1$ J/cm^2, $\tau_p = 1.0$ ms).

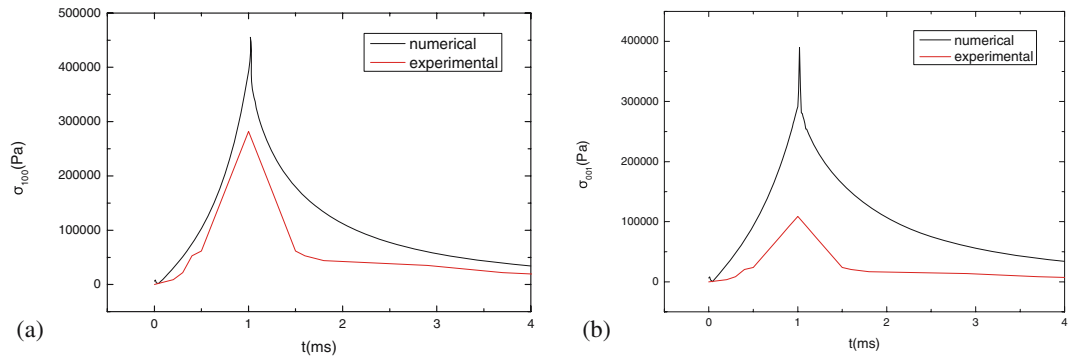

Figure 14. Comparison of curves of stress evolution between the experimental and the numerical results ($E_p = 10.1$ J/cm^2, $\tau_p = 1.0$ ms) (**a**) [1 0 0] and (**b**) [0 0 1] directions.

The experimental result is not completely in agreement with the numerical result, which may be due to two factors. Firstly, the physical parameters have errors in numerical simulation. Absorption coefficient and thermal conductivity are sensitive to stress and both absorption coefficient and thermal conductivity change with the rise of temperature during laser irradiation. But the relationship between the parameter changes and temperature does not exactly match with that of the experiments in simulation. Besides, spot in the simulation is in the shape of Gaussian distribution, whereas it is only in the shape of approximate Gaussian distribution in experiments. Secondly, the sample used in simulation is the ideal crystal while the samples used in experiments have impurities. Impurities can absorb heat, intensifying thermal diffusion. So the stress value is lower in experiments than in simulation. But the experimentally measured stress tendencies of σ_x, σ_z at the silicon surface are basically consistent with the ones that are calculated with the numerical model (figure 15).

As shown in figures 16–19, while laser fluence is 10.1 J/cm^2 and pulse width is 1 ms, the stress of lasing action centre will increase and then begin to decrease as the time increases and the stress generated near the centre is almost the same with that of the centre. Maximum stress occurs at the end of laser action, with the maximum stress reaching 3.0 $\times$ 10^5 Pa. With the increase of laser irradiation time, the depth of dislocation extends inwards. The measured maximum value of radial stress is 2.86 $\times$ 10^5 Pa and axial stress is 1.1 $\times$ 10^5 Pa. Both radial and axial stresses are tensile stresses. For the laser pulse widths 1.5 ms, 2 ms, 2.5 ms, stress of lasing action centre increases and then begins to decrease with the increase of time. The stress continues to decrease as it

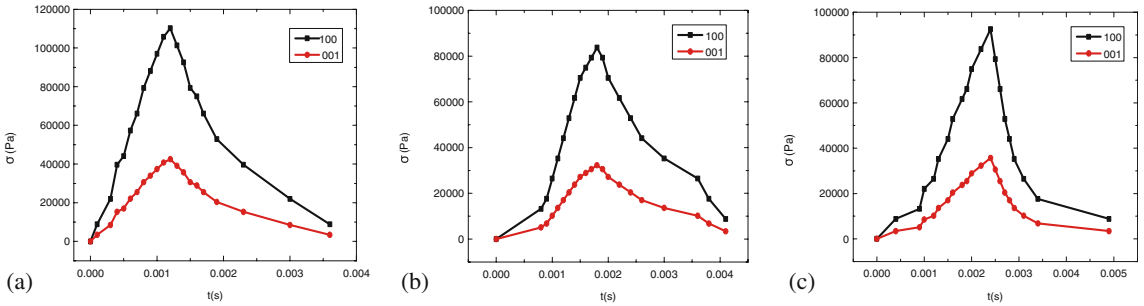

Figure 15. Details of stress evolutions of the spot centre for different pulse widths and laser fluences corresponding to [1 0 0] direction and [0 0 1] direction ((**a**) $E_p = 9.9$ J/cm^2, $\tau_p = 1.5$ ms, (**b**) $E_p = 10.3$ J/cm^2, $\tau_p = 2$ ms, (**c**) $E_p = 10.6$ J/cm^2, $\tau_p = 2.5$ ms).

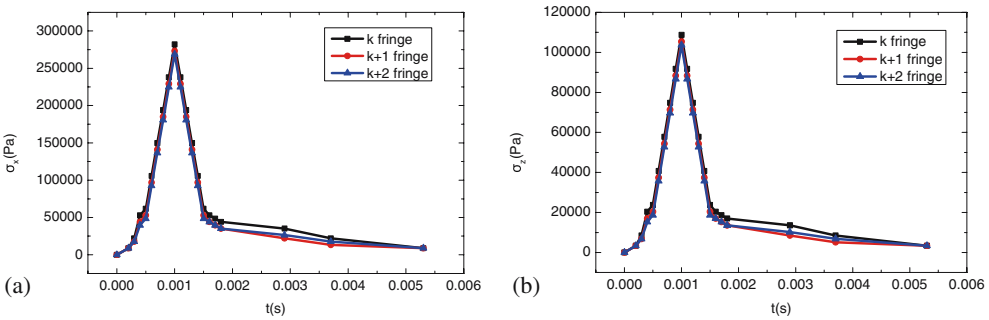

Figure 16. Time dependence of (**a**) radial and (**b**) axial stress on the silicon surface for different interference fringes ($E_p = 10.1$ J/cm^2, $\tau_p = 1.0$ ms).

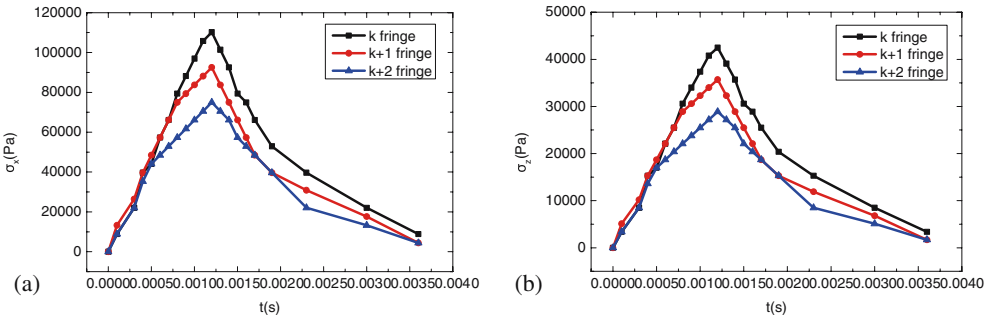

Figure 17. Time dependence of (**a**) radial and (**b**) axial stress on the silicon surface for different interference fringes ($E_p = 9.9$ J/cm^2, $\tau_p = 1.5$ ms).

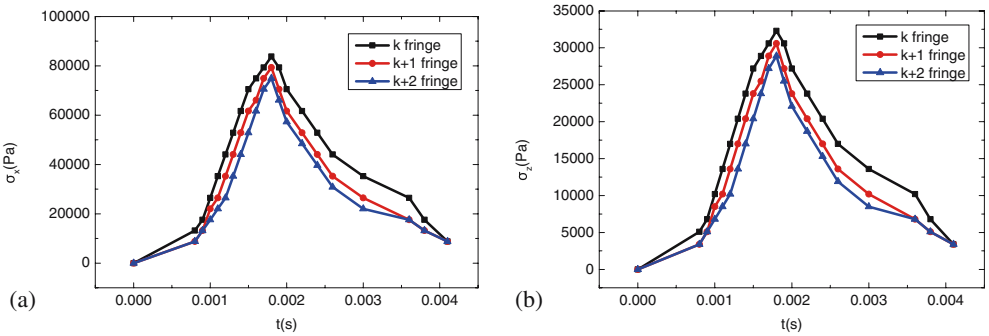

Figure 18. Time dependence of (**a**) radial and (**b**) axial stress on the silicon surface for different interference fringes ($E_p = 10.3$ J/cm^2, $\tau_p = 2$ ms).

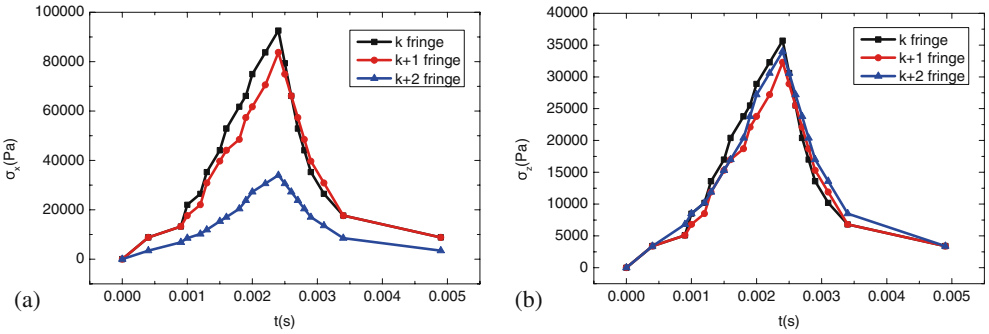

Figure 19. Time dependence of (**a**) radial and (**b**) axial stress on the silicon surface for different interference fringes ($E_p = 10.6\ \mathrm{J/cm^2}$, $\tau_p = 2.5$ ms).

gets farther from the centre position. Maximum stress occurs when the laser action ends. When the laser irradiation stops, monocrystalline silicon reaches the cooling stage, during which period the stresses manifest as tensile stresses. Stress concentration will appear in the dislocation defects. Therefore, only a small tensile stress can cause the extension of these crack points.

4. Conclusions

In summary, we have presented the stress measurement of monocrystalline silicon using the Mach–Zehnder interferometer technique. The effect of laser heating of monocrystalline silicon on the stress measurement was studied experimentally and numerically. Maximum stress occurs when laser action ends, the maximum shear stress in the direction [1 1 0] exists near the spot radius and [1 1 1] exists in the centre of spot. Both radial and axial stresses are tensile stresses. The spatial distribution of [1 1 1] shear stress has the characteristics of axial symmetry, but the [1 1 0] direction does not have that characteristics. As time increases, stress of lasing action centre first increases and then decreases. The experimentally measured tendencies are basically consistent with the ones which are calculated with the numerical model. It verifies the reliability of the numerical model. The results in this paper offer theoretical and experimental basis for further applications of silicon, especially for those studies on nanostructures formed by stress on bulk silicon. It can also significantly improve the performance of silicon-integrated circuits which have stress-related problems. Moreover, stress evolution can provide reference for the study of silicon fracture.

References

[1] F Östlund *et al*, *Adv. Funct. Mater.* **19(15)**, 2439 (2009)
[2] W Qiu *et al*, *Appl. Phys. Lett.* **92(4)**, 041906 (2008)
[3] S J Harris *et al*, *J. Appl. Phys.* **96(12)**, 7195 (2004)
[4] J Y Yen and J G Hwu, *J. Appl. Phys.* **89(5)**, 3027 (2001)
[5] Y Calahorra *et al*, *Nano Lett.* **15(5)**, 2945 (2015)
[6] P O Bouchard, M Bernacki and D M Parks, *Comput. Mater. Sci.* **69**, 243 (2013)
[7] X J Chen *et al*, *J. Crystal Growth* **310(19)**, 4330 (2008)
[8] X Wu *et al*, *Microelectron. J.* **38(1)**, 87 (2007)
[9] R K Endo, Y Fujihara and M Susa, *High Temp. High Press* **35**, 505 (2003)
[10] K Yamaguchi and K Itagaki, *J. Therm. Anal. Calor.* **69**, 1059 (2002)
[11] I D Vrinceanu and S Danyluk, Measurement of residual stress in single crystal silicon wafers, *Proceedings of the 8th IEEE International Symposium on Advanced Packaging Materials* (2002)
[12] R F Wood, C W White and R T Young, Pulsed laser processing of semiconductors, in: *Semiconductors and semimetals* (Academic Press, New York, 1984) Vol. 23
[13] Z Li *et al*, *J. Appl. Phys.* **114(3)**, 033104 (2013)
[14] W Z Li, B H Huang and Z B Bi, *Theoretical analysis and application of thermal stress* (Electric Power Press of China, Beijing, 2004) Vol. 76